



Multiple-models predictions for drip line nuclides in projectile fragmentation of $^{40,48}\text{Ca}$, $^{58,64}\text{Ni}$, and $^{78,86}\text{Kr}$ at 140 MeV/u

Xiao-Bao Wei¹ · Hui-Ling Wei¹ · Yu-Ting Wang¹ · Jie Pu¹ · Kai-Xuan Cheng¹ ·
Ya-Fei Guo¹ · Chun-Wang Ma¹

Received: 9 July 2022 / Revised: 29 October 2022 / Accepted: 30 October 2022 / Published online: 7 December 2022

© The Author(s), under exclusive licence to China Science Publishing & Media Ltd. (Science Press), Shanghai Institute of Applied Physics, the Chinese Academy of Sciences, Chinese Nuclear Society 2022

Abstract Modern rare isotope beam (RIB) factories will significantly enhance the production of extremely rare isotopes (ERI) at or near drip lines. As one of the most important methods employed in RIB factories, the production of ERIs in projectile fragmentation reactions should be theoretically improved to provide better guidance for experimental research. The cross-sections of ERIs produced in 140 MeV/u $^{78,86}\text{Kr}/^{58,64}\text{Ni}/^{40,48}\text{Ca} + ^9\text{Be}$ projectile fragmentation reactions were predicted using the newly proposed models [i.e., Bayesian neural network (BNN), BNN + FRACS, and FRACS, see Chin. Phys. C, 46: 074104 (2022)] and the frequently used EPAX3 model. With a minimum cross-section of 10^{-15} mb, the possibilities of ERIs discovery in a new facility for rare isotope beams (FRIB) are discussed.

Keywords Bayesian neural network (BNN) · FRACS · Drip line · Extremely rare isotope · Projectile fragmentation

1 Introduction

The newly predicted number of bounded nuclei is more than 9035 [1, 2], most of which are rare nuclei far away from the β -stable line. It is claimed that 3330 and 3340 nuclides have been discovered in web counting [3] and NUBASE2020 [4], while another 3000 with large isospin (or n/p asymmetry) are expected to be discovered in the new generation of rare isotope beam (RIB) factories [5, 6], which will double the number of known nuclides and expand the knowledge of nuclear structure, fundamental interaction, and nuclear astrophysics. Particularly, the new Facility for Rare Isotope Beams (FRIB) announced its opening on May 2nd, 2022, which can produce the extremely rare isotope (ERI) of lifetime as short as 10^{-21} second (zeptosecond) [7]. The news indicates that a variety of ERIs will be artificially created in the near future.

With cutting-edge technologies of enhanced primary beams or rare isotope beams and improved online particle identification systems in the new generation of RIB factories, ERIs in different mass regions can be produced through nuclear reactions of fission, fusion, nuclear spallation, multinucleon transfer, and projectile fragmentation (PF) reactions [8–12]. A projectile fragmentation reaction means that the accelerated projectile nuclear beam (stable or unstable) bombards the target nucleus, in which rare isotopes can be formed after violent collisions between the projectile and target nuclei. In the second generation of RIB factories, the accelerated beams are stable nuclei, and isospin effects have an observable influence on fragment production [13], that is, the production of neutron-rich fragments is enhanced in the reaction induced by the more neutron-rich projectile nucleus, and vice versa [14]. In the

This work was supported by the National Natural Science Foundation of China (No. 11975091) and the Program for Innovative Research Team (in Science and Technology) in University of Henan Province, China (No. 21IRTSTHN011).

✉ Chun-Wang Ma
machunwang@126.com

¹ College of Physics, Henan Normal University, Xixiang 453007, China

third generation of RIB factories, well-separated rare isotope (with large asymmetry) beams make it easier to produce ERIs at or near drip lines. The proof-of-principle experiment with a post-accelerated isotope separator online beam at the Beijing Radioactive Ion-beam Facility (BRIF) provided a powerful method for investigating ERIs and precious technology for the Huizhou accelerator complex facility under construction [15, 16]. For the new chance provided by the third generation of RIB factories to discover ERIs, most of existing theoretical models are not precise to describe rare isotopes of low productive rates (see the recent review in [6]). Some new methods, which are developed based on the empirical phenomena of fragment production in PF reactions, shed light on the high-quality prediction of rare fragments with large n/p asymmetry. For example, the FRACS formula [17] and its improved version FRACS-C (improved prediction quality for neutron-deficient fragments as well as the fragments in the PF reaction with incident energy below 100 MeV/u) [18], the scaling formula of fragment cross-sections [19], the relation of odd-even staggering laws [20–22], and the correlation between the fragment cross-section and average binding energy [23–25]. Following the success of machine learning models for predicting fragment production in spallation reactions, which have been constructed using Bayesian neural network technology (BNN) [26–28], BNN and BNN + FRACS models have been constructed for high-quality prediction of fragment production in PF reactions [29]. The constructed BNN and BNN + FRACS models for PF reactions are stimulated to simulate their cross-sections to determine the probabilities of EIRs with Z ranging from 4 to 27 that can be produced for the FRIB experimental exploration.

In this study, a multi-model prediction of cross-sections for ERIs in typical reactions (i.e., $^{78,86}\text{Kr}/^{58,64}\text{Ni}/^{40,48}\text{Ca} + ^9\text{Be}$ at 140 MeV/u) was performed using EPAX3, FRACS, BNN, and BNN + FRACS models. These models are briefly described in Sect. 2. In Sect. 3, the predicted cross-sections for fragments in the $^{78,86}\text{Kr}/^{58,64}\text{Ni}/^{40,48}\text{Ca} + ^9\text{Be}$ reactions are presented, in which we also discuss the possibility to discover new isotopes in experiments at FRIB. The summary of this paper is provided in Sect. 4.

2 Model descriptions

In this section, the adopted theoretical methods, including EPAX3 [30], FRACS [17], BNN, and BNN+FRACS [29], are briefly introduced. For a detailed description, readers are referred to the original articles.

By employing as many measured fragment cross-sections in projectile fragmentation reactions as that in 2012, a

universal empirical formula EPAX3 [30] was proposed based on its previous version EPAX2 [31], aiming at a better quality for most neutron-rich fragments by maintaining good quality for neutron-deficient fragments. In EPAX3, it is assumed that the fragment yields are independent of the incident energy of the reaction when it is above the Fermi energy (approximately 40 MeV/u), but a suitable range of incident energy is suggested to be above 140 MeV/u [28]. EPAX2 and EPAX3 are important methods for fragment prediction in PF and spallation reactions for intermediate and relativistic energies [6, 28].

The FRACS formulas [17] modified the EPAX3 formulas by implanting the energy dependence and odd-even staggering factors for fragment production, and the prediction accuracy significantly improved. With a new set of parameters, it is assumed to be efficient for predicting ERIs in PF reactions with incident energies above 100 MeV/u. In a recent comprehensive comparison using measured data for reaction systems from intermediate projectile nuclei to heavy ones, FRACS formulas illustrate a high-quality prediction for fragment cross-sections [29]. A thorough description of FRACS formulas can be found in [17].

The BNN and BNN + FRACS models have been constructed [29] to precisely predict fragment cross-sections in projectile fragmentation reactions. The model structures of the BNN and BNN + FRACS are one input layer with seven input parameters, one output layer with one output parameter, and optimized 46 neural units in one hidden layer. The BNN model was constructed by direct learning of the massive fragment cross-sections measured (6393 data in 53 reactions; see Supplementary Information in [29]), while the BNN + FRACS model was constructed by learning and minimizing the difference between the FRACS prediction and measured results. With a large number of learning datasets assembled, the constructed BNN and BNN + FRACS models can predict fragment cross-sections for reactions with incident energies from 40 to 1000 MeV/u, projectile nuclei from approximately ^{40}Ar to ^{208}Pb , and fragments of mass (A_f) from the light ones to those around the projectile nucleus ($5 \leq A_f \leq A_p$). The advantages of the BNN and BNN + FRACS models make it possible to predict the production of ERIs in projectile fragmentation reactions induced by both stable and rare nuclei. The description of the BNN and BNN + FRACS models can be found in [29].

3 Results and discussion

Considering the advantages of FRIB nuclear beams, projectile fragmentation reactions of 140 MeV/u $^{78,86}\text{Kr} + ^9\text{Be}$, $^{58,64}\text{Ni} + ^9\text{Be}$, and $^{40,48}\text{Ca} + ^9\text{Be}$ were simulated using

the EPAX3, FRACS, BNN, and BNN + FRACS models. The enhanced beam intensity of the FRIB produces more neutron-rich ERIs, although their cross-sections are extremely low. The discussion is grouped as follows:

- The global production for fragments.
- ERIs on the neutron-rich side in $^{48}\text{Ca} + ^9\text{Be}$, $^{64}\text{Ni} + ^9\text{Be}$, and $^{86}\text{Kr} + ^9\text{Be}$ reactions.
- ERIs on the neutron-deficient side in $^{40}\text{Ca} + ^9\text{Be}$, $^{58}\text{Ni} + ^9\text{Be}$, and $^{78}\text{Kr} + ^9\text{Be}$ reactions.

3.1 Global production for fragments

The predicted cross-sections for fragments were compared among 140 MeV/u $^{78,86}\text{Kr} + ^9\text{Be}$, $^{58,64}\text{Ni} + ^9\text{Be}$, and $^{40,48}\text{Ca} + ^9\text{Be}$ reactions. For isotopes from $Z = 1$ to 12, the maximum cross-sections produced in $^{40,48}\text{Ca}$ and $^{58,64}\text{Ni}$ reactions were selected, whereas the maximum cross-sections in $^{40,48}\text{Ca}$, $^{58,64}\text{Ni}$, and $^{78,86}\text{Kr}$ reactions were selected to plot the figures for those of $Z > 12$.

Following the assumption in the previous study [29], with the lowest limitation of 10^{-15} mb, the fragments with cross-sections above were discussed. In Fig. 1, the predicted fragments with cross-sections larger than 10^{-15} mb have been plotted in the form of a nuclear landscape, and shown ones have the maximum cross-section in the six predicted reactions. The nuclides in light gray denote those predicted in AME2020 [32], while those in light blue denote the range from the LISE++ toolkit-implanted dataset of FRIB [33]. The predicted results of the four models show that the distribution of the dominant fragments produced by the six projectiles is divided into two parts, and the dividing line almost coincides with the β -stable line. The production of fragments on the neutron-rich side is dominated by ^{48}Ca , ^{64}Ni , and ^{86}Kr reactions. Above the stable line, fragments can be produced in ^{40}Ca , ^{58}Ni , and ^{78}Kr reactions. In panels (b) and (c), the fragments for $Z \leq 4$ and $N \leq 8$ have larger cross-sections in the ^{40}Ca reaction. With the lowest limitation of 10^{-15} mb, neutron-deficient isotopes for elements $Z \leq 28$ can be reached using ^{40}Ca and ^{58}Ni projectiles at 140 MeV/u. For the reaction induced by ^{78}Kr , the fragments produced were considerably close to the proton drip line.

On the neutron-rich side of the landscape, in the $^{48}\text{Ca} + ^9\text{Be}$ reaction, the fragments can reach the drip line of $Z \leq 11$ of AME2020, whereas for those of $12 \leq Z \leq 14$, only isotopes close to the neutron drip line of AME2020 could be found. Fragments with $Z \geq 15$ have the maximum cross-sections in the $^{86}\text{Kr} + ^9\text{Be}$ reaction. For the predicted

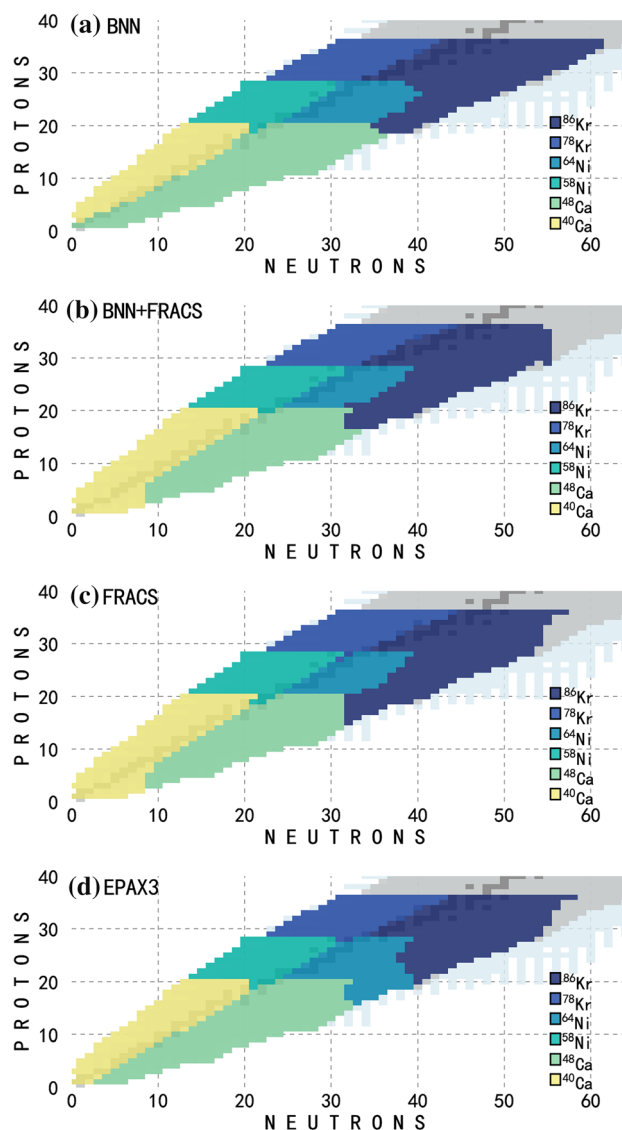


Fig. 1 (Color Online) Landscapes for predicted fragments with cross-sections larger than 10^{-15} mb in 140 MeV/u $^{78,86}\text{Kr} + ^9\text{Be}$, $^{58,64}\text{Ni} + ^9\text{Be}$ and $^{40,48}\text{Ca} + ^9\text{Be}$ reactions. Panels a–d show that nuclides have the maximum cross-section in the predicted reactions by BNN, BNN + FRACS, FRACS, and EPAX3 models, respectively

existing limitations of $Z \leq 12$ by LISE++ for the FRIB, the predicted isotopes could not cover this region. In general, on the neutron-rich side of the landscape, it is observed that the BNN predicts more nuclides than FRACS, and BNN + FRACS predicts fewer nuclides than FRACS. Although EPAX3 predicts a similar number of isotopes to other methods, the production of neutron-rich isotopes for Z from 15 to 20 is dominated by the $^{64}\text{Ni} + ^9\text{Be}$ reaction, which is different from those of the BNN, BNN + FRACS, and FRACS models.

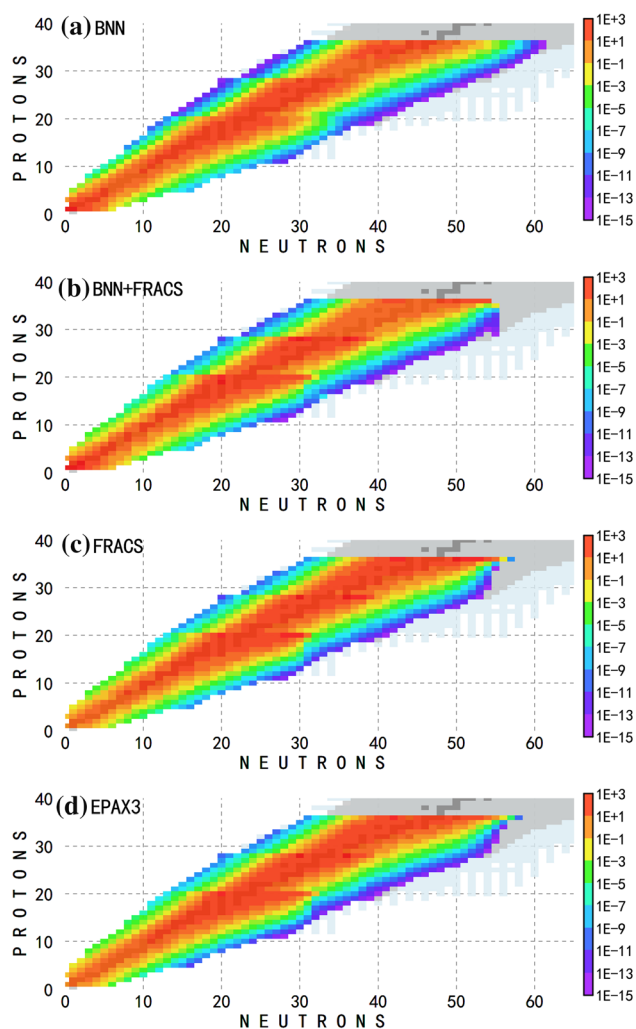


Fig. 2 (Color Online) Contour plots according to Fig. 1 but for fragment cross-sections predicted by BNN, BNN + FRACS, and FRACS models, in which the lowest cross-section is above 10^{-15} mb

The corresponding contour plots according to the cross-sections of the fragments presented in Fig. 1 are drawn in Fig. 2. For proton drip line isotopes of $Z \leq 36$, they are prospective to be produced using the ^{40}Ca , ^{58}Ni and ^{78}Kr primary beams both predicted by BNN, BNN + FRACS, FRACS and EPAX3 models, except that BNN has much lower cross-sections than those of BNN + FRACS and FRACS models. For isotopes on the neutron-rich side of the chart, all four models cover the AME2020 prediction for $Z \leq 28$. For the area close to the projectile ^{86}Kr , only the BNN results show that it is possible to produce the drip-line nuclei predicted by AME2020. All four models cover the range of neutron-rich ones with Z from 1 to 11 for the LISE++ predicted isotopes for the FRIB. For isotopes of $Z \geq 12$, the predictions by the four models cannot reach

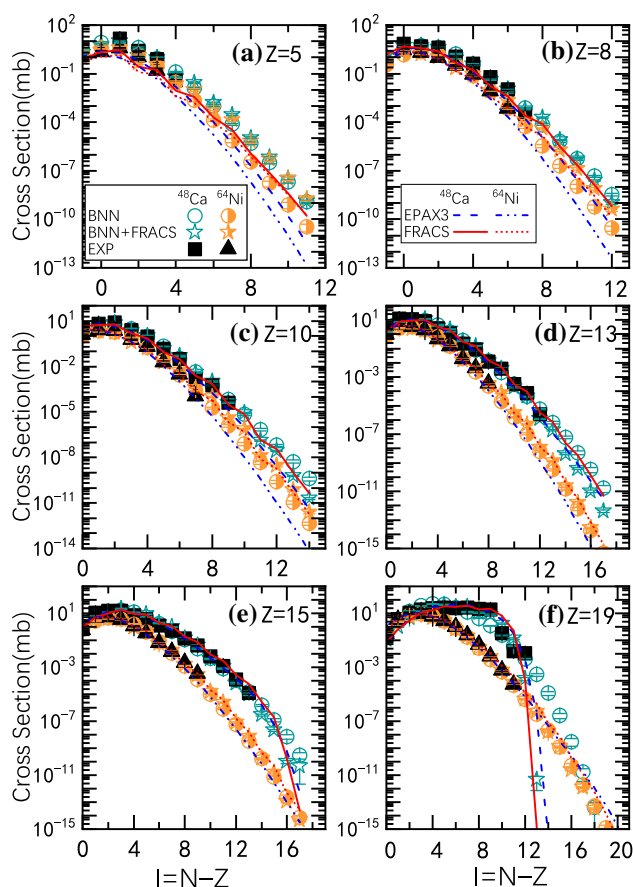


Fig. 3 (Color online) Predicted cross-sections for neutron-rich fragments in 140 MeV/u $^{48}\text{Ca} + ^9\text{Be}$ and $^{64}\text{Ni} + ^9\text{Be}$ reactions as a function of the neutron excess of fragment ($I = N - Z$). The measured data for fragments are obtained in [36]

the neutron-rich edge by LISE++ predictions for the FRIB.

3.2 ERIs on neutron-rich Side

For the ERIs on the neutron-rich side, fragments at 140 MeV/u $^{48}\text{Ca} + ^9\text{Be}$, $^{64}\text{Ni} + ^9\text{Be}$, and $^{86}\text{Kr} + ^9\text{Be}$ reactions are plotted in Figs. 3 and 4. Additional data for the reactions at 140 MeV/u are listed in Table 1 in Appendix.

The first experimental exploration of new isotopes at FRIB aimed at the discovery of new half-lives of EIRs on the neutron-rich side from magnesium to phosphorus, mainly using the projectile of ^{48}Ca [34, 35]. Similar measurements were performed during the first decade of the 21th century [36]. For these ERIs, the predicted cross-sections for fragments produced in 140 MeV/u $^{48}\text{Ca} + ^9\text{Be}$ and $^{64}\text{Ni} + ^9\text{Be}$ reactions were compared with the measured data presented in Fig. 3. In general, the four models

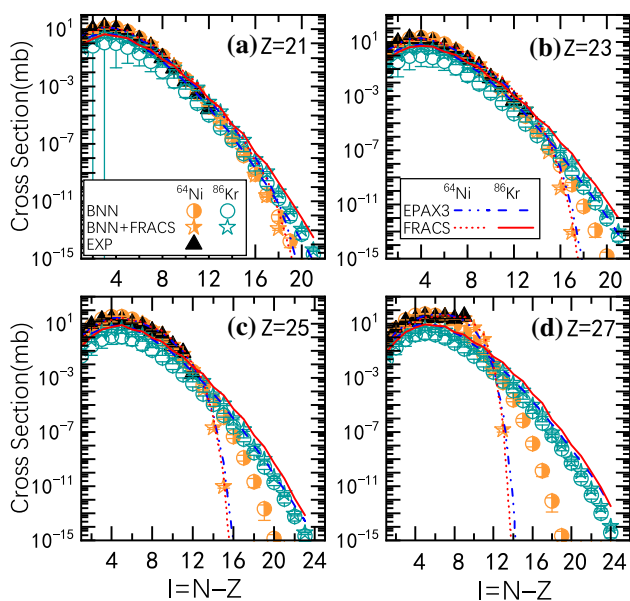


Fig. 4 (Color online) Similar plots as Fig. 3 but for neutron-rich fragments in 140 MeV/u $^{64}\text{Ni} + ^9\text{Be}$ and $^{86}\text{Kr} + ^9\text{Be}$ reactions

accurately predicted the measured data. This discussion focuses on neutron-rich ERIs production. The experiments confirmed that the nuclei along the $A = 3Z + 4$ line up to $Z = 13$ are bounded, except for the ^{28}O , ^{25}N , and ^{16}Be isotopes. The latest work at RIKEN first observed the new isotope ^{39}Na beyond the experiential line in the light mass range with the estimated cross-section (0.5 fb) being very close to the BNN prediction (0.46 fb) [37]. For ERIs with $Z \geq 10$, the cross-sections in the ^{48}Ca reaction are larger than those in the ^{64}Ni reaction, and the BNN prediction results are clearly higher than those of the other models. A reasonable extrapolation trend of isotopic distributions can be obtained by the four models; however, the EPAX3, FRACS, and BNN+FRACS predictions rapidly drop when the fragments are close to the projectile ^{48}Ca . In EPAX3 and FRACS, the quick drop is caused by the “brute-force” factor. It down-scales the predicted cross-section to fit the experimental data and depends on the neutron excess of the projectile and the fragment nucleus. The BNN + FRACS prediction is also influenced by this because it is rooted in the FRACS. Thus, the new discovery of ERIs should address the shortcoming of the BNN + FRACS model.

In Fig. 4, the isotopic cross-sections for fragments are compared for the 140 MeV/u $^{64}\text{Ni} + ^9\text{Be}$ and $^{86}\text{Kr} + ^9\text{Be}$ reactions, which use neutron-rich projectiles. Similar phenomena to those shown in Fig. 3 (f) can be found in Figs. 4 (c) and (d), that is, a quick drop is shown in EPAX3, FRACS,

and BNN + FRACS predictions for ERIs with mass numbers considerably close to that of projectile (^{64}Ni).

3.3 ERIs on neutron-deficient side

In a recent work, a discussion on the production of neutron-deficient nuclei with $Z = 20 - 25$ in the framework of isospin-dependent Boltzmann–Langevin model using the radioactive $^{48-59}\text{Ni}$ beams at 140, 240, and 345 MeV/u [38], showed that the cross-section of neutron-deficient nuclei could be significantly enhanced by neutron-deficient projectiles. For stable neutron-deficient primary beams, it is necessary to investigate the possibility of ERIs production near proton drip lines.

For ERIs on the neutron-deficient side, the fragments at 140 MeV/u $^{40}\text{Ca} + ^9\text{Be}$, $^{58}\text{Ni} + ^9\text{Be}$, and $^{78}\text{Kr} + ^9\text{Be}$ reactions are plotted in Figs. 5 and 6. Additional data for the reactions at 140 MeV/u are listed in Table 2 in Appendix.

In Fig. 5, fragments from $Z = 6$ to 18 are compared for 140 MeV/u $^{40}\text{Ca} + ^9\text{Be}$ and $^{58}\text{Ni} + ^9\text{Be}$ reactions. It is easy to find that the predicted cross-sections by BNN and BNN + FRACS are in very good agreement with the measured data, while EPAX3 and FRACS underestimated the light fragments that were far away from the projectiles, as shown in panel (a). The extrapolation of the ERIs near the proton drip line shows that the projectile ^{40}Ca is a better choice. The predictions of ERIs by the EPAX3, FRACS, and BNN + FRACS models are close, whereas the BNN predictions for fragments on the proton-rich side with $I \leq -3$ are smaller than those of the other models. The ERIs for the neutron-deficient isotopes of $Z \geq 20$ in 140 MeV/u $^{58}\text{Ni} + ^9\text{Be}$ and $^{78}\text{Kr} + ^9\text{Be}$ reactions are compared in Fig. 6. The EPAX3, FRACS, and BNN + FRACS predictions are similar, while the BNN prediction is much lower than the other models. It should be noted that all fragments with $I = -7$ for $Z = 9 - 27$ elements could be reached in the reactions predicted by the adopted models, providing new opportunities to study exotic multi-proton emissions in extreme neutron-deficient nuclei [39].

4 Summary

FRACS, BNN, and BNN + FRACS models, and EPAX3 formulas were adopted to predict the ERI cross-sections in typical PF reactions of 140 MeV/u $^{78,86}\text{Kr} + ^9\text{Be}$, $^{58,64}\text{Ni} + ^9\text{Be}$, and $^{40,48}\text{Ca} + ^9\text{Be}$ reactions for the FRIB factory. A global comparison of ERI production is

Table 1 The predicted cross-sections (in mb) of light neutron-rich fragment by BNN(σ_{BN}), BNN + FRACS(σ_{BF}), FRACS(σ_{FR}), and EPAX3(σ_{EP}) in 140 MeV/u $^{48}\text{Ca} + ^9\text{Be}$ reactions

Frag.		140 MeV/u				
Z	I	σ_{BN}	σ_{BF}	σ_{FR}	σ_{EP}	
9	10	(19.3±2.65) E-07	(15.0±1.49) E-07	9.71E-07	1.62E-07	
9	11	(17.4±2.75) E-08	(21.3±2.28) E-08	1.61E-07	7.59E-09	
9	12	(14.6±2.79) E-09	(37.0±4.34) E-10	3.40E-09	3.07E-10	
9	13	(11.2±2.67) E-10	(13.1±1.71) E-11	1.51E-10	1.08E-11	
10	10	(67.8±8.72) E-07	(82.5±7.75) E-07	7.12E-06	9.18E-07	
10	11	(6.83±1.02) E-07	(13.4±1.36) E-08	1.38E-07	5.26E-08	
10	12	(6.37±1.15) E-08	(27.4±3.08) E-09	3.50E-08	2.60E-09	
10	13	(5.39±1.23) E-09	(61.0±7.72) E-11	1.00E-09	1.13E-10	
10	14	(4.05±1.18) E-10	(19.2±2.78) E-12	4.22E-11	4.30E-12	
11	10	(24.4±2.89) E-06	(11.0±1.00) E-06	1.21E-05	5.22E-06	
11	11	(27.4±3.78) E-07	(26.1±2.58) E-07	3.52E-06	3.64E-07	
11	12	(28.4±4.79) E-08	(43.5±4.74) E-09	7.40E-08	2.21E-08	
11	13	(26.6±5.66) E-09	(10.0±1.23) E-09	2.25E-08	1.18E-09	
11	14	(22.0±5.99) E-10	(11.4±1.62) E-11	3.53E-10	5.57E-11	
11	15	(15.6±5.48) E-11	(32.3±5.38) E-13	1.44E-11	2.37E-12	
11	16	(9.35±4.19) E-12	(7.23±1.42) E-14	4.82E-13	9.09E-14	
11	17	(4.59±2.62) E-13	(13.1±3.04) E-16	1.35E-14	3.21E-15	
12	10	(89.3±9.57) E-06	(11.1±1.00) E-05	1.51E-04	2.95E-05	
12	11	(11.2±1.40) E-06	(30.8±2.99) E-07	5.22E-06	2.51E-06	
12	12	(12.8±1.98) E-07	(57.6±6.16) E-08	1.27E-06	1.87E-07	
12	13	(13.2±2.57) E-08	(8.89±1.07) E-09	2.64E-08	1.23E-08	
12	14	(11.9±2.98) E-09	(11.9±1.67) E-10	5.03E-09	7.26E-10	
12	15	(9.12±2.94) E-10	(25.2±4.17) E-12	1.57E-10	3.91E-11	
12	16	(5.76±2.40) E-11	(7.09±1.40) E-13	6.75E-12	2.02E-12	
12	17	(2.92±1.57) E-12	(18.9±4.35) E-15	2.59E-13	1.03E-13	
13	10	(32.9±3.17) E-05	(20.3±1.83) E-05	3.30E-04	1.65E-04	
13	11	(45.9±5.17) E-06	(43.4±4.18) E-06	9.01E-05	1.71E-05	
13	12	(58.2±8.03) E-07	(12.4±1.30) E-07	3.42E-06	1.57E-06	
13	13	(6.55±1.14) E-07	(18.6±2.21) E-08	7.16E-07	1.30E-07	
13	14	(6.34±1.42) E-08	(42.7±5.94) E-10	2.41E-08	1.02E-08	
13	15	(5.11±1.49) E-09	(39.5±6.55) E-11	3.36E-09	7.69E-10	
13	16	(3.31±1.27) E-10	(10.6±2.07) E-12	1.28E-10	5.33E-11	
13	17	(16.7±8.40) E-12	(41.5±9.18) E-14	4.92E-12	2.59E-12	
14	10	(12.2±1.06) E-04	(16.6±1.51) E-04	3.14E-03	9.15E-04	
14	11	(18.9±1.90) E-05	(88.8±8.46) E-06	2.20E-04	1.18E-04	
14	12	(26.3±3.20) E-06	(17.5±1.81) E-06	5.94E-05	1.41E-05	
14	13	(31.8±4.86) E-07	(67.8±7.99) E-08	3.33E-06	1.59E-06	
14	14	(32.4±6.41) E-08	(8.04±1.13) E-08	5.91E-07	1.66E-07	
14	15	(26.6±7.00) E-09	(16.0±2.68) E-10	1.68E-08	1.32E-08	
14	16	(17.0±6.01) E-10	(21.7±4.19) E-11	2.23E-09	5.85E-10	
14	17	(8.05±3.85) E-11	(4.30±1.20) E-12	8.42E-12	9.12E-12	
15	10	(45.5±3.63) E-04	(42.3±3.82) E-04	9.13E-03	5.26E-03	
15	11	(77.7±7.01) E-05	(10.6±0.99) E-04	3.09E-03	9.06E-04	
15	12	(11.6±1.25) E-05	(67.1±6.87) E-06	2.79E-04	1.43E-04	
15	13	(14.8±1.99) E-06	(9.47±1.13) E-06	5.85E-05	1.84E-05	
15	14	(15.3±2.70) E-07	(28.9±4.19) E-08	2.55E-06	1.53E-06	
15	15	(12.3±2.96) E-08	(21.1±3.62) E-09	1.83E-07	5.91E-08	
15	16	(7.27±2.44) E-09	(9.93±2.60) E-11	1.67E-10	5.98E-10	
15	17	(3.02±1.42) E-10	(4.53±4.32) E-11	2.43E-14	5.95E-13	
16	10	(16.8±1.26) E-03	(36.2±3.21) E-03	8.84E-02	3.34E-02	

Table 1 continued

Frag.		140 MeV/u			
Z	I	σ_{BN}	σ_{BF}	σ_{FR}	σ_{EP}
16	11	(31.0±2.58) E-04	(33.3±3.09) E-04	1.15E-02	6.91E-03
16	12	(48.6±4.76) E-05	(56.0±5.92) E-05	2.83E-03	1.06E-03
16	13	(62.4±7.72) E-06	(19.5±2.51) E-06	1.41E-04	9.39E-05
16	14	(6.22±1.04) E-06	(7.45±1.17) E-07	5.33E-06	3.24E-06
16	15	(4.55±1.07) E-07	(24.4±6.13) E-10	3.48E-09	2.13E-08
16	16	(23.1±7.77) E-09	(10.1±9.03) E-11	4.91E-14	6.95E-12
16	17	(7.65±3.68) E-10	(3.74±19.8) E-08	5.20E-26	7.58E-18

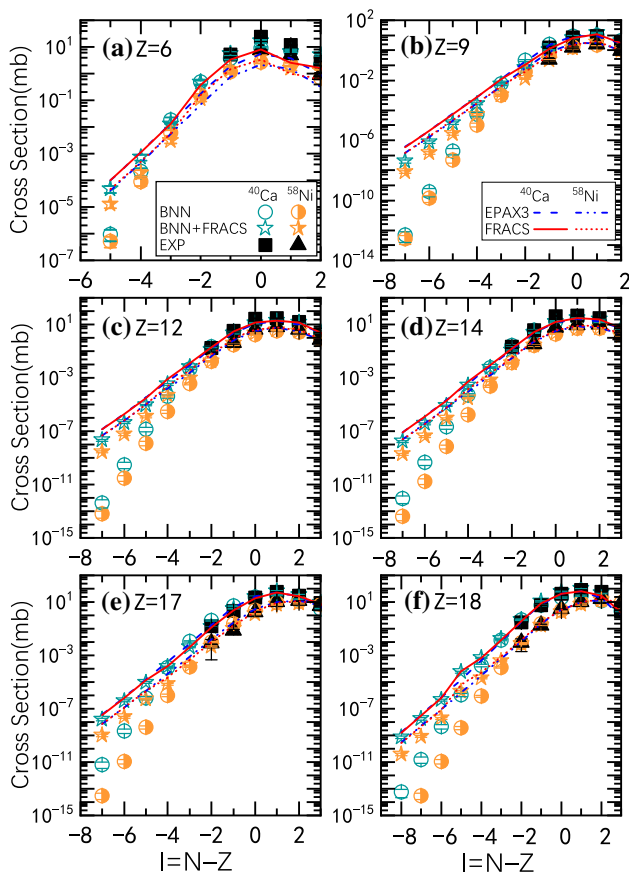


Fig. 5 (Color online) Predicted cross-sections for neutron-deficient fragments produced in 140 MeV/u $^{40}\text{Ca} + ^9\text{Be}$ and $^{58}\text{Ni} + ^9\text{Be}$ reactions as a function of the neutron excess of fragment ($I = N - Z$). The measured data for fragments are obtained in [36]

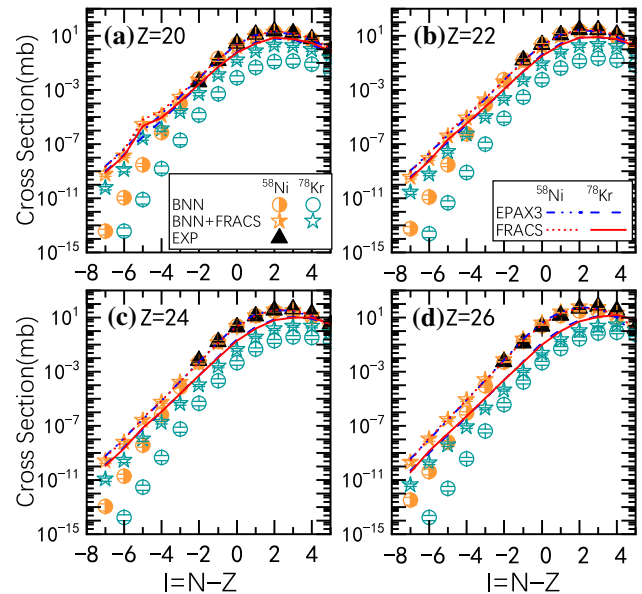


Fig. 6 (Color online) Similar plots as in Fig. 5 but for neutron-deficient fragments produced in 140 MeV/u $^{58}\text{Ni} + ^9\text{Be}$ and $^{78}\text{Kr} + ^9\text{Be}$ reactions

made among the four models, showing that with the lowest cross-section of 10^{-15} mb, both neutron and proton drip lines can be reached for elements of $Z \leq 11$. We discussed neutron-rich ERI fragments in the reactions of neutron-rich projectiles ^{48}Ca , ^{64}Ni , and ^{86}Kr as well as neutron-deficient ERI fragments in the reactions of neutron-deficient projectiles ^{40}Ca , ^{58}Ni , and ^{78}Kr . It was found that model predictions could reproduce the measured data, whereas the

Table 2 The predicted cross-sections (in mb) of light proton-rich fragment by BNN(σ_{BN}), BNN+FRACS(σ_{BF}), FRACS(σ_{FR}), and EPAX3(σ_{EP}) in 140MeV/u $^{40}\text{Ca} + ^9\text{Be}$ reactions

Frag.	140 MeV/u				
Z	I	σ_{BN}	σ_{BF}	σ_{FR}	σ_{EP}
9	-7	(4.93±3.38) E-13	(39.9±9.41) E-09	3.53E-07	3.60E-07
9	-6	(3.79±2.14) E-10	(7.32±1.47) E-07	4.28E-06	4.39E-06
9	-5	(19.7±8.68) E-08	(13.9±2.38) E-06	5.54E-05	5.72E-05
9	-4	(5.27±1.70) E-05	(27.0±3.97) E-05	7.61E-04	7.90E-04
9	-3	(5.76±1.26) E-03	(53.5±6.88) E-04	1.10E-02	1.15E-02
9	-2	(21.5±3.07) E-02	(68.8±7.92) E-03	1.08E-01	1.77E-01
10	-7	(4.01±2.67) E-13	(29.8±6.25) E-09	2.57E-07	2.65E-07
10	-6	(3.01±1.65) E-10	(5.76±1.04) E-07	3.32E-06	3.45E-06
10	-5	(15.6±6.65) E-08	(11.4±1.77) E-06	4.56E-05	4.76E-05
10	-4	(4.32±1.33) E-05	(22.9±3.11) E-05	6.60E-04	6.92E-04
10	-3	(4.98±1.02) E-03	(8.67±1.05) E-03	1.86E-02	1.06E-02
11	-7	(3.86±2.48) E-13	(24.1±4.69) E-09	1.88E-07	1.96E-07
11	-6	(2.78±1.46) E-10	(48.5±8.17) E-08	2.58E-06	2.71E-06
11	-5	(14.2±5.74) E-08	(9.90±1.46) E-06	3.73E-05	3.93E-05
11	-4	(3.95±1.14) E-05	(20.5±2.67) E-05	5.66E-04	6.00E-04
11	-3	(47.1±8.95) E-04	(24.3±2.87) E-04	5.10E-03	9.58E-03
12	-7	(4.36±2.68) E-13	(20.7±3.85) E-09	1.39E-07	1.46E-07
12	-6	(2.95±1.47) E-10	(42.9±6.97) E-08	2.01E-06	2.13E-06
12	-5	(14.5±5.50) E-08	(8.98±1.29) E-06	3.04E-05	3.24E-05
12	-4	(3.98±1.06) E-05	(31.7±4.07) E-05	8.06E-04	5.16E-04
12	-3	(48.1±8.27) E-04	(64.8±7.60) E-04	1.28E-02	8.60E-03
13	-8	(8.72±6.13) E-16	(8.84±1.84) E-10	7.11E-09	7.53E-09
13	-7	(5.72±3.35) E-13	(18.5±3.36) E-09	1.03E-07	1.09E-07
13	-6	(3.56±1.67) E-10	(39.2±6.25) E-08	1.56E-06	1.67E-06
13	-5	(16.4±5.80) E-08	(8.40±1.18) E-06	2.47E-05	2.66E-05
13	-4	(4.36±1.06) E-05	(11.3±1.44) E-05	2.56E-04	4.43E-04
13	-3	(52.2±8.02) E-04	(27.0±3.15) E-04	4.86E-03	7.71E-03
14	-8	(1.49±1.01) E-15	(7.95±1.63) E-10	5.03E-09	5.38E-09
14	-7	(8.63±4.81) E-13	(17.1±3.05) E-09	7.63E-08	8.22E-08
14	-6	(4.82±2.12) E-10	(36.9±5.81) E-08	1.21E-06	1.31E-06
14	-5	(20.5±6.69) E-08	(8.07±1.13) E-06	2.01E-05	2.19E-05
14	-4	(5.12±1.14) E-05	(27.3±3.44) E-05	5.37E-04	3.83E-04
14	-3	(59.3±8.23) E-04	(55.9±6.45) E-04	8.94E-03	6.99E-03
15	-8	(2.98±1.94) E-15	(7.34±1.49) E-10	3.59E-09	3.89E-09
15	-7	(14.9±7.89) E-13	(16.1±2.87) E-09	5.72E-08	6.23E-08
15	-6	(7.29±3.02) E-10	(35.7±5.59) E-08	9.55E-07	1.05E-06
15	-5	(27.8±8.46) E-08	(8.01±1.11) E-06	1.67E-05	1.84E-05
15	-4	(6.41±1.31) E-05	(11.6±1.45) E-05	1.95E-04	3.38E-04
15	-3	(70.2±9.05) E-04	(28.6±3.27) E-04	4.00E-03	6.55E-03
16	-8	(6.88±4.36) E-15	(6.95±1.41) E-10	2.61E-09	2.86E-09
16	-7	(2.90±1.48) E-12	(15.7±2.79) E-09	4.38E-08	4.83E-08
16	-6	(12.2±4.82) E-10	(35.9±5.61) E-08	7.73E-07	8.56E-07
16	-5	(4.10±1.18) E-07	(8.35±1.16) E-06	1.44E-05	1.60E-05
16	-4	(8.51±1.65) E-05	(32.7±4.08) E-05	4.63E-04	3.15E-04
16	-3	(8.63±1.08) E-03	(73.5±8.41) E-04	8.85E-03	6.59E-03
17	-8	(1.83±1.13) E-14	(6.82±1.40) E-10	1.96E-09	2.17E-09

Table 2 continued

Frag.	140 MeV/u				
Z	I	σ_{BN}	σ_{BF}	σ_{FR}	σ_{EP}
17	-7	(6.38±3.15) E-12	(16.0±2.88) E-09	3.50E-08	3.90E-08
17	-6	(22.6±8.63) E-10	(38.3±6.08) E-08	6.62E-07	7.42E-07
17	-5	(6.53±1.82) E-07	(9.46±1.33) E-06	1.33E-05	1.50E-05
17	-4	(12.0±2.28) E-05	(13.8±1.75) E-05	1.63E-04	3.24E-04
17	-3	(11.0±1.41) E-03	(42.9±5.00) E-04	4.37E-03	7.59E-03

predicted results for ERI fragments with large asymmetry may have significant differences. It can be concluded that many new isotopes can be created in the new FRIB factory, making it possible to enlarge the nuclear landscape and reveal their exotic phenomena.

Appendix

The predicted cross-sections (in mb) by the BNN, BNN + FRACS, FRACS, and EPAX3 models are listed in this section. Tables 1 and 2 summarize the results for neutron-rich (see Sect. 3.2) and neutron-deficient fragments (see Sect. 3.3), respectively.

Author Contributions All authors contributed to the study conception and design. Material preparation, data collection and analysis were performed by Xiao-Bao Wei and Chun-Wang Ma. The first draft of the manuscript was written by Xiao-Bao Wei, and all authors commented on previous versions of the manuscript. All authors read and approved the final manuscript.

References

- K. Zhang, M.K. Cheoun, Y.B. Choi et al., Nuclear mass table in deformed relativistic Hartree-Bogoliubov theory in continuum, I: even-even nuclei. *Atom. Data Nucl. Data Tabl.* **144**, 101488 (2022). <https://doi.org/10.1016/j.adt.2022.101488>
- X.W. Xia, Y. Lim, P.W. Zhao et al., The limits of the nuclear landscape explored by the relativistic continuum Hartree-Bogoliubov theory. *Atom. Data Nucl. Data Tabl.* **121–122**, 1–215 (2018). <https://doi.org/10.1016/j.adt.2017.09.001>
- Discovery of nuclides project. <https://people.nsl.msui.edu/thoennes/isotopes/> Accessed 30 Nov. 2022
- F.G. Kondev, M. Wang, W.J. Huang et al., The NUBASE2020 evaluation of nuclear physics properties. *Chin. Phys. C* **45**, 030001 (2021). <https://doi.org/10.1088/1674-1137/abddae>
- T. Baumann, M. Hausmann, B.M. Sherrill et al., Opportunities for isotope discovery at the FRIB. *Nucl. Instrum. Meth. Phys. Res. B* **376**, 33 (2016). <https://doi.org/10.1016/j.nimb.2016.02.057>
- C.W. Ma, H.L. Wei, X.Q. Liu et al., Nuclear fragments in projectile fragmentation reactions. *Prog. Part. Nucl. Phys.* **121**, 103911 (2021). <https://doi.org/10.1016/j.pnpnp.2021.103911>
- The facility for rare isotope beams opens its doors to discovery. <https://msutoday.msu.edu/news/2022/frib-grand-opening>
- A. Gade, T. Glasmacher, In-beam nuclear spectroscopy of bound states with fast exotic ion beams. *Prog. Part. Nucl. Phys.* **60**, 161 (2008). <https://doi.org/10.1016/j.pnpnp.2007.08.001>
- T. Nakamura, H. Sakurai, H. Watanabe, Exotic nuclei explored at in-flight separators. *Prog. Part. Nucl. Phys.* **97**, 53 (2017). <https://doi.org/10.1016/j.pnpnp.2017.05.001>
- F. Niu, P.H. Chen, H.G. Cheng et al., Multinucleon transfer dynamics in nearly symmetric nuclear reactions. *Nucl. Sci. Tech.* **31**, 59 (2020). <https://doi.org/10.1007/s41365-020-00770-1>
- R. Li, D.H. Zhang, Measurement of cross sections for charge pickup by ^{84}Kr on Al, C and CH_2 targets at 400 MeV/u. *Nucl. Sci. Tech.* **31**, 58 (2020). <https://doi.org/10.1007/s41365-020-00768-9>
- J. Wei, H. Ao, B. Arend et al., Accelerator commissioning, and rare isotope identification at the facility for rare isotope beams. *Mod. Phys. Lett. A* **37**, 2230006 (2022). <https://doi.org/10.1142/S0217732322300063>
- C.C. Guo, J. Su, L. Zhu, Secondary decay effects of isospin fractionation on projectile fragmentation at GeV/nucleon. *Nucl. Sci. Tech.* **31**, 123 (2020). <https://doi.org/10.1007/s41365-020-00832-4>
- C.W. Ma, Y.P. Liu, H.L. Wei et al., Determination of neutron skin thickness using configurational information entropy. *Nucl. Sci. Tech.* **33**, 6 (2022). <https://doi.org/10.1007/s41365-022-00997-0>
- W. Nan, B. Guo, C.J. Lin et al., First proof-of-principle experiment with the post-accelerated isotope separator online beam at BRIF: measurement of the angular distribution of $^{23}\text{Na} + ^{40}\text{Ca}$ elastic scattering. *Nucl. Sci. Tech.* **32**, 53 (2021). <https://doi.org/10.1007/s41365-021-00889-9>
- H.W. Zhao, H.S. Xu, G.Q. Xiao et al., Huizhou accelerator complex facility and its future development. *Sci. China-Phys. Mech. Astron.* **50**, 112006 (2020). <https://doi.org/10.1360/SSPMA-2020-0248>. (in Chinese)
- B. Mei, Improved empirical parameterization for projectile fragmentation cross sections. *Phys. Rev. C* **95**, 034608 (2017). <https://doi.org/10.1103/PhysRevC.95.034608>
- Y.D. Song, H.L. Wei, C.W. Ma et al., Improved FRACS parameterizations for cross sections of isotopes near the proton drip line in projectile fragmentation reactions. *Nucl. Sci. Tech.* **29**, 96 (2018). <https://doi.org/10.1007/s41365-018-0439-4>
- Y.D. Song, H.L. Wei, C.W. Ma, A scaling phenomenon for the cross section of fragment produced in projectile fragmentation reactions. *Sci. China-Phys. Mech. Astron.* **62**, 992011 (2019). <https://doi.org/10.1007/s11433-018-9364-x>
- J.R. Winkelbauer, S.R. Souza, M.B. Tsang, Influence of secondary decay on odd-even staggering of fragment cross

- section. Phys. Rev. C **88**, 044613 (2013). <https://doi.org/10.1103/PhysRevC.88.044613>
21. B. Mei, Accurate odd-even staggering relations for fragmentation and spallation cross section. Phys. Rev. C **103**, 044610 (2021). <https://doi.org/10.1103/PhysRevC.103.044610>
 22. B. Mei, Odd-even staggering for production cross-sections of nuclei near the neutron drip-line. Chin. Phys. C **45**, 084109 (2021). <https://doi.org/10.1088/1674-1137/ac06ab>
 23. M.B. Tsang, W.G. Lynch, W.A. Friedman et al., Fragmentation cross sections and binding energies of neutron-rich nuclei. Phys. Rev. C **76**, 041302 (2007). <https://doi.org/10.1103/PhysRevC.76.041302>
 24. C.W. Ma, Y.D. Song, H.L. Wei, Binding energies of near proton drip line $Z = 22-28$ isotopes determined from measured isotopic cross section distributions. Sci. China-Phys. Mech. Astron. **62**, 012013 (2019). <https://doi.org/10.1007/s11433-018-9256-8>
 25. Y.D. Song, H.L. Wei, C.W. Ma, Fragmentation binding energies and cross sections of isotopes near the proton dripline. Phys. Rev. C **98**, 024620 (2018). <https://doi.org/10.1103/PhysRevC.98.024620>
 26. C.W. Ma, D. Peng, H.L. Wei et al., Isotopic cross-sections in proton-induced spallation reactions based on the Bayesian neural network method. Chin. Phys. C **44**, 014104 (2020). <https://doi.org/10.1088/1674-1137/44/1/014104>
 27. C.W. Ma, D. Peng, H.L. Wei et al., A Bayesian-neural-network prediction for fragment production in proton induced spallation reaction. Chin. Phys. C **44**, 124107 (2020). <https://doi.org/10.1088/1674-1137/abb657>
 28. D. Peng, H.L. Wei, X.X. Chen et al., Bayesian evaluation of residual production cross sections in proton-induced nuclear spallation reactions. J. Phys. G- Part. Nucl. Phys. **49**, 085102 (2022). <https://doi.org/10.1088/1361-6471/ac7069>
 29. C.W. Ma, X.B. Wei, X.X. Chen et al., Precise machine learning models for fragment production in projectile fragmentation reactions using Bayesian neural networks. Chin. Phys. C **46**, 074104 (2022). <https://doi.org/10.1088/1674-1137/ac5efb>
 30. K. Stümmerer, Improved empirical parametrization of fragmentation cross section. Phys. Rev. C **86**, 014601 (2012). <https://doi.org/10.1103/PhysRevC.86.014601>
 31. K. Stümmerer, B. Blank, modified empirical parameterization of fragmentation cross sections. Phys. Rev. C **61**, 034607 (2000). <https://doi.org/10.1103/PhysRevC.61.034607>
 32. M. Wang, W.J. Huang, F.G. Kondev et al., AME 2020 Atomic Mass Evaluation (II) Tables, graphs, and references. Chinese Phys. C **45**, 030003 (2021). <https://doi.org/10.1088/1674-1137/abddaf>
 33. LISE++ cute, <https://lise.nslc.msu.edu/lise.html>
 34. FRIB's first experiment concludes successfully, <https://frib.msu.edu/news/2022/first-experiment.html>
 35. H.L. Crawford, V. Tripathi, J.M. Allmond et al., Crossing $N = 28$ toward the neutron drip-line: First measurement of half-lives at FRIB. Phys. Rev. Lett. **129**, 212501 (2022). <https://doi.org/10.1103/PhysRevLett.129.212501>
 36. M. Mocko, M.B. Tsang, L. Andronenko et al., projectile fragmentation of ^{40}Ca , ^{48}Ca , ^{58}Ni , and ^{64}Ni at 140 MeV/nucleon. Phys. Rev. C **74**, 054612 (2006). <https://doi.org/10.1103/PhysRevC.74.054612>
 37. D.S. Ahn, J. Amano, H. Baba et al., Discovery of ^{39}Na . Phys. Rev. Lett. **129**, 212502 (2022). <https://doi.org/10.1103/PhysRevLett.129.212502>
 38. B. Li, N. Tang, F.S. Zhang, Production of p-rich nuclei with $Z = 20 - 25$ based on radioactive ion beams. Nucl. Sci. Tech. **33**, 55 (2022). <https://doi.org/10.1007/s41365-022-01048-4>
 39. L. Zhou, S.M. Wang, D.Q. Fang et al., Recent progress in the two-proton radioactivity. Nucl. Sci. Tech. **33**, 105 (2022). <https://doi.org/10.1007/s41365-022-01091-1>
- Springer Nature or its licensor (e.g. a society or other partner) holds exclusive rights to this article under a publishing agreement with the author(s) or other rightsholder(s); author self-archiving of the accepted manuscript version of this article is solely governed by the terms of such publishing agreement and applicable law.